Addressing Visualization of X-Ray Images: Toward an AI-Based Post-processing Strategy for Enhanced Image Presentation Quality

Sonja Pappenberger, Peter Keuschnigg, Phillip Steiniger, and Daniel Sieber

***Abstract*—The employment of artificial intelligence (AI) and in particular its subset deep learning (DL), has opened up a variety of possibilities for novel approaches in multiple fields, including medical image analysis. One of the key tasks in this domain is image enhancement, which is of particular importance for x-ray images, as they frequently suffer from poor image quality due to noise, scattering, blurring, or low contrast. Window-leveling is an image enhancement technique that is often employed to improve the visual representation of an image.**

In this study, we present an AI-based approach for automatically adjusting of the window-leveling parameters of two-dimensional (2D) x-ray images. In order to predict the parameters, a convolutional neural network was employed. The model was optimized in two phases. Initially, selected training hyperparameters were optimized, namely the batch size, the optimizer and its learning rate. Subsequently, its architecture was optimized. Accordingly, the model's architecture was successively simplified to minimize the required computational time for predicting the window-leveling parameters.

The proposed network comprises one convolutional layer and two fully-connected layers to generate the window-leveling parameters. The mean square error for the two parameters, namely the window-width and the window-level, was 0.0033 and 0.0013, respectively, and the mean absolute percentage error was 4.61%/5.16%, respectively.

The proposed model demonstrated robust performance in automatic window-leveling adjustment of 2D x-ray images and offers space for further investigation.

***Index Terms*—Deep Learning, Convolutional Neural Network, Window-Leveling, X-ray Images, Image Enhancement.**

I. Introduction

ARTIFICIAL intelligence (AI) is currently a tool utilized for a multitude of practical applications across various fields, including language processing, automation of routine tasks, as well as image analysis [1]. The recent rapid developments of this technology can be attributed to three key factors: advances in the development of high-performance computing hardware, an increase in the availability of data for training the AI models, as well as a progress in the development of learning algorithms [1], [2], [3]. In medical image analysis, in particular the employment of deep learning (DL), a subset of AI [1], has lead to the development of novel approaches to several key tasks in this domain [4]. These key tasks include image registration, image reconstruction, image segmentation, computer-aided detection and diagnosis, as well as image enhancement [4].

The implementation of DL has the potential to enhance the efficiency of clinical workflows by automating routing tasks [5]. For example, DL technology can assist radiologists in their daily decision-making processes by detecting and classifying pathological findings in medical images or by giving statements about the progression of certain diseases, such as the extent of tumorous tissue [4]. Moreover, the integration of DL technology has been demonstrated to improve the accuracy of diagnostic predictions. The predictions made by human experts supported by DL technology were more accurate than those made by either humans or DL technology alone [6]. Another benefit of employing DL technology in the field of medical image analysis is an enhanced image quality while reducing the scanning time or the radiation dose, thereby increasing patient safety [4], [7], [8].

One of the principal technologies in medical image analysis is image enhancement [4], whereby the objective is to increase the quality of an image. This is especially required for x-ray images as they frequently suffer from poor quality due to factors such as noise, scattering, blurring and low contrast. The reason for this is the high scanning complexity of the body tissues which arises during radiography [9]. Traditional enhancement techniques to increase the contrast of an x-ray image include methods such as histogram equalization (HE) and the application of the contrast limited adaptive histogram equalization (CLAHE) filter. When applying HE to an image, the pixel values of the images are redistributed in order to achieve a more uniform distribution of the pixel intensity values [10], [11], [12]. Also the CLAHE filter performs the HE operation in a first step. However, in the CLAHE filter, HE is not applied to the entire image at once, but to discrete image tiles, subregions of the images. In addition, the contrast is limited with the objective to reduce noise amplification in the image. Finally, CLAHE performs bilinear interpolation to provide smooth transitions between the distinct image tiles [13]. A third technique to increase the quality of an x-ray image is window-leveling, a linear intensity transformation that improves the visibility of structures within a specific region of interest in the image. Window-leveling maps the pixel values of an image within a defined intensity range. The operation sets the pixel values below the lower boundary of the specified range to black and assigns the brightest possible

S. Pappenberger is with the Department of Medical and Health Technologies, MCI, Innsbruck, Austria

P. Keuschnigg is with medPhoton GmbH, Salzburg, Austria.

P. Steiniger is with medPhoton GmbH, Salzburg, Austria.

D. Sieber is with the Department of Medical and Health Technologies, MCI, Innsbruck, Austria, e-mail: daniel.sieber@mci.edu

Manuscript received July 31, 2024;

display value to pixel values exceeding the upper limit of the range [10]. The displayed range is defined by a window-level (WL) wl and a window-width (WW) ww, whereby WL represents the value in the middle of WW. WW is defined by a lower limit w_{low} and an upper limit w_{up}. Consequently, WW is calculated by $ww = w_{up} - w_{low}$ and WL by $wl = \frac{w_{up}+w_{low}}{2}$ [10], [14].

The most traditional and straightforward method for performing window-leveling is manual [15]. However, this approach is energy-intensive and time-consuming [4].

Consequently, algorithms to automatically adjust window-leveling parameters, i.e. the values for WW and WL, have been developed. Examples can be found in the literature and can be divided into two groups: those that use traditional techniques and those that use AI-based technology.

Examples for approaches that employ traditional image processing techniques include the algorithm, presented by Tan et al. The proposed method automatically adjusts WW and WL not for medical images, but for high-dynamic industrial x-ray images. The algorithm is based on the short-term energy of the gray level histogram. When tested in practice, the developed algorithm demonstrated robust performance [15]. Hoeschen et al. proposed in their study an algorithm to adapt the WW and WL values in medical x-ray images containing implants. This algorithm is also based on the gray level histogram, as it detects the border between the gray level block of anatomical structures and the grey level block of artificial structures. Subsequently, the detected border is set to 90% of the brightest displayable value [16]. Another method, designated as the GRAIL (Gabor-relying adjustment of image levels) algorithm, was presented by Albiol et al. Their developed methodology iteratively adjusts the gray level values of mammographic images based on a perceptual metric, utilizing special filters, namely the Gabor filters [17]. Yeganeh et al. proposed a window-leveling methodology for medical images that employs a structural fidelity measure, which assesses image quality. With their algorithm they overcome the limitations of window-leveling based on linear gray level mapping [18]. Nikvand et al. also presented an approach for adaptive window-leveling of medical images. Their approach involves an information-theoretic measure based on the concept of normalized information distance, in conjunction with the theory of Kolmogorov complexity [19]. MedPhoton GmbH (hereafter referred to as "medPhoton") employs an automatic window-leveling (AWL) algorithm using two distinct approaches. In the first approach, the window is set from the minimum pixel value of the image to the maximum pixel value. In the second approach, the window is defined by a threshold that depends on the frequency of the pixel value that occurs most frequently in the image. Depending on the x-ray imaging modality, the first or the second approach is applied. Nevertheless, in the past, these two approaches have resulted in some instances in unsatisfactory visual representations of the images.

As previously stated, AI technology has also been employed in the development of window-leveling methods. Early work includes the two-stage neural network, presented by Ohhashi et al. in 1991, to compute the window-leveling parameters for magnetic resonance (MR) images. The proposed algorithm includes the extraction of features from the gray level histogram of the images [20]. In 2000, Lai and Fang employed a hierarchical neural network to adjust the WW and WL values for MR images. Their network uses features extracted from the wavelet histogram in addition to spatial statistical information [21]. In 2005, the same authors proposed an advanced method to automatically adjust the window-leveling parameters of MR images, making it more adaptive to different viewing conditions [22]. A common limitation of the aforementioned AI-based window-leveling methods is the necessity of feature extraction prior to computing the WW and WL values. The algorithm proposed by Zhao et al. addressed this limitation by employing a convolutional neural network (CNN) for window-leveling adjustment. As CNNs can directly extract features from the input image, the need of prior feature extraction was eliminated [14]. However, also this approach was limited to MR images. Another methods for the automatic window-leveling adjustment of MR images was proposed by Sundaran et al. Their approach differs from the aforementioned method, as is suppresses in a first step the background pixels of the MR image using a DL model. Subsequently, the foreground pixels are window-leveled using a non-AI-based algorithm. However, Sundaran et al. did not provide further description of this approach [23].

A review of the literature reveals that the majority of automatic window-leveling approaches, particularly those based on AI, are constrained to MR images. To the best of our knowledge, no study has yet presented an AI-based algorithm for predicting optimal WW and WL values for x-ray images.

This paper proposes an AI-based approach for automatically adjusting the window-leveling parameters of two-dimensional (2D) x-ray images by employing a DL model. A convolutional neural network (CNN) is employed in order to predict optimal window-leveling parameter, i.e., the values for WW and WL. These predicted parameters can then be utilized to visualize the x-ray image. This AI-based approach should, in the long term, provide an alternative to medPhoton's established window-leveling algorithms.

II. Methods

A. Software and hardware

The programming language utilized was Python (version 3.8.18, Python Software Foundation). The open-source Python libraries PyTorch [24] and TorchIO [25] were employed for training the model and for pre-processing the x-ray images, respectively [26]. Training was performed on a NVIDIA graphics processing unit (GPU), namely the NVIDIA RTX 3500 Ada Generation Laptop GPU, utilizing the CUDA (compute unified device architecture) toolkit (version 11.3.1). In the C++ environment, the model was tested on a NVIDIA RTX A2000 8G laptop GPU.

B. Dataset

A dataset of 800 anonymized x-ray images, provided by medPhoton, was selected, covering various anatomical regions, including the pelvis, breast, lung, abdomen, cochlea, and the

spine. The dataset was randomly split into three subsets: a training dataset, a validation dataset, and a testing dataset with a split ratio of 0.7/0.15/0.15. Accordingly, the network was trained on 559 x-ray images, validated on 121 images, and tested on 120 images. To ensure reproducibility, a manual seed of 42 was set.

For labeling the selected x-ray images, medPhoton's AWL algorithm was applied on them. As all images in the dataset may be used for marketing purposes at medPhoton, it was ensured that the AWL algorithm resulted in a satisfactory visual representation. For this reason, a certain level of quality for the computed values for WW and WL was reasonably assumed, so that these values were employed as labels for the dataset.

C. Image pre-processing

Prior to being fed into the DL model, the images underwent several pre-processing steps. In a first step, it was ensured that the input image was stored in transmission space, given that x-ray images are, in some cases, for efficiency reasons, stored as a ushort, an unsigned integer data type. Transmission space, however, ranges from $(0, 1)$. A pixel value of zero indicates that no radiation was detected by the x-ray detector and that all radiation was absorbed by the imaged object. In contrast, a pixel value of one in transmission space indicates that all radiation was detected by the x-ray detector and no radiation was absorbed by the imaged object.

Rescaling to transmission space transforms the ushort integer pixel value p_{int} linearly to its floating point transmission value p_{float} by using the rescale intercept $i_{rescale}$ and the rescale slope $s_{rescale}$. These two parameters are stored in the metadata of the x-ray images. Mathematically, rescaling to transmission space is described by the following equation:

$$p_{float} = p_{int} * s_{rescale} + i_{rescale} \tag{1}$$

Consequently, also the WW and WL values that were used as labels had to lie within the range of $(0, 1)$. This was ensured by reviewing the computed label values.

The implementation of that first pre-processing steps guarantees that, regardless of the x-ray image that is input to the model (including x-rays that are not part of the dataset), its pixel values are stored in the same image space. Simultaneously, the input is normalized, as the transmission space ranges from zero to one.

In the second pre-processing step, the image was cropped to size of the x-ray collimator, ensuring that only the relevant section of the image was processed by the DL model. The final step involved resizing the image to the input size of the model. Figure 2 in Appendix A illustrates the various pre-processing steps.

D. Deep learning model

As DL model a CNN was employed. Its architecture was inspired by the work of Jiang et al. [27], who also proposed a CNN for predicting multiple continuous numerical values from an input image. However, the context of their study differed from that of the present paper. The output layer of the model presented by Jiang et al. was modified since only two output values were required for the purpose of the present paper, namely the WW and the WL value. The architecture of the model is depicted in Figure 1. As illustrated in the figure, the CNN model comprised five convolutional blocks. Each block included batch normalization following the convolution, the rectified linear unit (ReLU) function as the activation function, and max pooling. Two fully-connected linear layers were subsequently employed to generate the output. The required dimensions of the input image for the model were $(C, H, W) = (1, 224, 224)$.

For training the DL model, the Huber function was selected as the loss function. Additionally, a baseline configuration of the following hyperparameters was selected: A batch size of 64 was utilized, and the Adam optimizer was selected with a learning rate of 0.001.

E. Evaluation and optimization of the model

The DL model was trained for 60 epochs with the baseline hyperparameter configuration. Following each training epoch, the model was validated and saved. After 60 epochs of training, the model with the lowest validation loss was selected and evaluated. To evaluate the selected model, the mean squared error (MSE) as well as the mean absolute percentage error (MAPE) were calculated. These measures were calculated for both outputs. Consequently, the MSE for WW and for WL was calculated, and the MAPE for WW and for WL, as mathematically expressed by following equations:

$$MSE_{ww} = \frac{1}{n}\sum_{i=1}^{n}(ww_i - \hat{ww}_i)^2 \tag{2}$$

MSE for WL:

$$MSE_{wl} = \frac{1}{n}\sum_{i=1}^{n}(wl_i - \hat{wl}_i)^2 \tag{3}$$

MAPE for WW:

$$MAPE_{ww} = \frac{1}{n}\sum_{i=1}^{n}\left|\frac{(ww_i - \hat{ww}_i)}{ww_i}\right| * 100 \tag{4}$$

MAPE for WL:

$$MAPE_{wl} = \frac{1}{n}\sum_{i=1}^{n}\left|\frac{(wl_i - \hat{wl}_i)}{wl_i}\right| * 100 \tag{5}$$

where $\hat{ww}$ and $\hat{wl}$ correspond to the predicted WW and WL values by the model and n to the number of samples in the dataset.

Subsequently, a series of hyperparameter configurations were tested. In each configuration, the model was trained for 60 epochs. The model with the lowest validation loss among the total 60 saved models was selected for evaluation. Table I provides an overview of the different variations of tested hyperparameters.

The model exhibiting the lowest evaluation metrics was selected for further optimization.

In the second phase of optimization, the architecture was reduced to the greatest extent possible while maintaining the

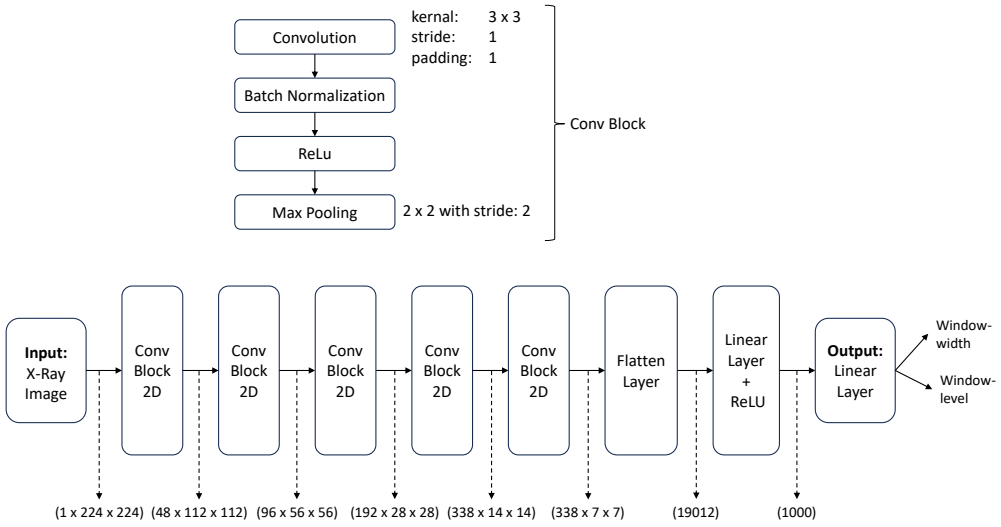

Fig. 1: Architecture of the customized CNN. Adapted from [27].

TABLE I: Overview of hyperparameter variations.

Hyperparameter	Baseline	Variation 1	Variation 2	Variation 3
Batch size	64	32	16	1
Optimizer	Adam	AdaDelta	SGD	RMSProp
Learning rate	0.001	0.1	0.01	0.0001

prediction accuracy as assessed by the evaluation metrics. The objective of this optimization step was to reduce the file size of the model to the greatest extent possible in order to enhance the computational speed of the model. The required computational time was tested in C++ environment, given that at medPhoton the majority of code runs in C++. For purposes of comparison, the average computational time of medPhoton's AWL algorithm was calculated utilizing the 120 x-ray images of the test dataset.

The subsequent table illustrates the downsized versions. The convolutional blocks were successively removed and the dimensions of the input image were additionally reduced.

TABLE II: Overview of downsized versions of the CNN.

Version	Convolutional blocks	Input size
A	5	224×224
B	4	112×112
C	3	56×56
D	2	28×28
E	1	14×14

III. Results

A. Baseline model

The model that was trained with the baseline configuration, which exhibited the lowest validation loss, resulted in the following evaluation metrics:

Figure 3 in Appendix B provides a visual representation of the predicted WW and WL values in comparison to the corresponding label WW and WL values.

TABLE III: Evaluation metrics for custom model.

MSE WW	MSE level	MAPE WW / %	MAPE level / %
0.0069	0.0050	8.4402	10.0396

B. Model optimization

Various hyperparameter configurations were assessed in order to optimize the model. Consequently, a single hyperparameter was modified at a time, and the resulting configuration was evaluated. In the event that a distinct variation of the hyperparameter, as compared to the baseline configuration, demonstrated superior predictive performance, as assessed by the evaluation metrics, this variation was then retained in subsequent configurations. This approach resulted in the tested hyperparameter configurations, which are presented in Table IV. The parameters that were compared in the single configurations are marked in blue. Table V presents the evaluation metrics that resulted for the different hyperparameter configurations. Figure 4 in Appendix B illustrates the comparison between the predicted WW and WL values of the model with optimized hyperparameter configuration and the WW and WL label values.

TABLE IV: Hyperparameter configurations during optimization.

Configuration	Batch size	Optimizer	Learning rate
1	64	Adam	0.001
2	32	Adam	0.001
3	16	Adam	0.001
4	1	Adam	0.001
5	16	AdaDelta	0.001
6	16	SGD	0.001
7	16	RMSProp	0.001
8	16	Adam	0.1
9	16	Adam	0.01
10	16	Adam	0.0001

TABLE V: Evaluation metrics for hyperparameter optimization configurations.

Conf.*	MSE WW	MSE WL	MAPE WW / %	MAPE WL / %
1	0.0069	0.0050	8.4402	10.0396
2	0.0040	0.0010	6.4083	4.0324
3	0.0029	0.0004	5.7240	2.4765
4	0.0202	0.0058	13.262	10.1583
5	0.0089	0.0052	9.5927	10.1583
6	0.0102	0.0086	9.9989	12.6719
7	0.0123	0.0085	12.3563	15.0363
8	0.0139	0.0121	14.0974	19.3825
9	0.0124	0.0022	12.5722	7.5410
10	0.0023	0.0006	3.0149	2.4980

* Configuration

With regard to the second optimization phase of the model, in which the architecture of the model was reduced to the greatest extent possible, the resulting number of parameters and file sizes are presented in Table VI.

TABLE VI: Numbers of parameters and file sizes of downsized models.

Version	Parameters	Size / MB
A	21 251 490	83.0
B	9 952 154	38.9
C	4 832 570	18.9
D	1 198 958	4.7
E	589 790	2.3

The evaluation metrics, as presented in Table VII, resulted from the distinct downsized model versions.

TABLE VII: Evaluation metrics for size optimization.

Vers.*	MSE WW	MSE WL	MAPE WW / %	MAPE WL / %
A	0.0023	0.0006	3.0149	2.4980
B	0.0031	0.0008	5.1493	3.2366
C	0.0027	0.0009	3.9129	3.8177
D	0.0025	0.0018	4.1020	5.2948
E	0.0033	0.0013	4.6136	5.1563

* Version

Figure 5 in Appendix B provides a further comparison between the label WW and WL values and the WW and WL values predicted by the model with the smallest architecture (version E).

With regard to the computational time, the models in version A and version E were tested in C++ environment. Version A required 7 milliseconds (ms) to predict the window-leveling parameters, whereas version E required only 3 ms. The average time for the AWL algorithm of medPhoton on the x-rays images of the test dataset was found to be 10 ms, with a range of 4 ms to 18 ms.

IV. Discussion

A. Main findings

A comparison of Figure 3 and Figure 4 reveals that hyperparameter optimization had a notable impact on the performance of the model. The dotted line, which represents the predicted WW and WL values of the model is in Figure 4 much closer to the solid line, representing the label values, than in Figure 3. This is supported by the evaluation metrics in Table V, which demonstrate that in the last configuration the metrics are notably smaller than those observed in the first configuration, which assessed the baseline configuration. Especially the selected batch size of 16 in the third configuration made an considerable difference as well as the selected learning rate of 0.0001. Consequently, the best results were obtained in the last configuration, where a batch size of 16 was utilized and the Adam algorithm as an optimizer with a learning rate of 0.0001. The evaluation metrics for this hyperparameter configuration were the lowest with a MSE WW/WL of 0.0023/0.0006 and a MAPE WW/WL of 3.01%/2.50%.

As evidenced in Table VII, the number of convolutional blocks in the CNN model proved to be a less important factor in the performance of the model than the training hyperparameter configuration. Despite successive reduction in the architecture, the model performance remained robust. The model with the smallest architecture still exhibited low evaluation metrics, with a MSE WW/WL of 0.0033/0.0013 and a MAPE WW/WL of 4.61%/5.16%. The number of parameters as well as the file size could be reduced by 97% for the smallest model in version E in comparison to the model in version A.

Please refer to Appendix C for the comparison between several example x-ray images visualized with the predictions of the distinct models: In the left column, the x-rays are visualized with the label WW and WL values, as computed by the AWL algorithm. The middle left column displays the images visualized with the parameters predicted by the baseline model. The middle right column visualized the x-rays with the parameters predicted by the model with optimized hyperparameter configuration and the right column visualizes the x-rays with the parameters predicted by the downsized model (version E). A comparsion of the columns reveals that no notable difference between the x-ray imges is visible.

Furthermore, progress was made with regard to the computational speed. A comparison of the required computational time of the AWL algorithm and the CNN model in version A revealed a reduction of 30% in the latter. In comparison of the AWL algorithm to the CNN model in version E, the required computational time was decreased by 70%.

B. Comparison to related literature

A comparison to the studies of Ohhashi et al. [20] and Lai et al. [21], [22] reveals that our AI-based window-leveling approach has the advantage of eliminating the need for prior feature extraction from the images, as this is done by the CNN model.

The results of this paper can also be compared to the study presented by Zhao et al. As previously mentioned, they proposed a CNN to predict the values for WW and WL for MR images [14]. The structure of the network presented by the authors comprised three principal components. In the first component, the dimensions of the input MR image were reduced. The second component of the network compromised five convolutional blocks, each containing three convolutional layers, with each layer followed by the ReLU activation

function and a pooling layer at the end of the block. In the third component, three fully-connected layers were employed to generate the two output values. In our study, the reduction of the dimensions of the input image is part of the pre-processing process. However, without considering the first component of their proposed network, their model remains notably more complex compared to our network.

Zhao et al. also employed MAPE as an evaluation metric for the predicted WW and WL values. When evaluated using this metric alone, our model demonstrated equal performance, with a MAPE a MAPE WW/WL of 4.61%/5.16% compared to a MAPE WW/WL of 4.72%/5.17% of the proposed model by Zhao et al. [14]. However, a direct comparison between the two models is challenging, given the distinct image characteristics of x-ray images and MR images [28]. To achieve a meaningful comparison, a more comprehensive analysis of these differences is necessary.

C. Limitations

One limitation of this study was the quality of the labels which were utilized during training the model. A simple window-leveling algorithm was employed to generate the labels. Their quality could be enhanced by manual window-leveling the x-ray images by a medical expert, such as a radiologist. However, this was not feasible within the scope of this paper. Nevertheless, through the use of x-ray images that may be employed for marketing purposes a certain quality level of the labels was ensured.

Moreover, it was not feasible to employ a radiologist to asses the results, i.e. the x-ray images visualized with the window-leveling parameters predicted by the developed model. This could be subjected to future studies.

A further limitation of this study was that it was constrained to 2D images. The developed network only enables AI-based window-leveling of 2D x-ray images. However, this opens up possibilities for future investigation, whereby the presented CNN network could be further developed to also enable window-leveling of three-dimensional (3D) x-rays, such as computed tomography images. Moreover, this study was limited by the fact that only images of one imaging modality were included, namely x-ray images. Networks have already been developed to enable AI-based window-leveling of MRI images [14], [23]. The subsequent step would be to develop a network that includes images of more than one imaging modality, enabling the enhancement in visual representation of images from various modalities, including, for example, radiography, MR imaging, and ultrasound imaging.

V. Conclusion

The objective of this paper was the development of an AI-based approach enabling automatic window-leveling adjustment of 2D x-ray images. This was achieved by employing a CNN model which was trained to predict optimal window-leveling parameters, i.e. values for WW and WL. The optimized CNN model comprised one convolutional block and two fully connected layers at the end, generating the output of the model.

The work shows promising results and can be used as a staring point for future work including further development of the presented network to enable window-leveling for a wider range of medical images, including 3D images as well as images of other imaging modalities.

Acknowledgment

The authors would like to thank everyone who contributed to this paper. A special thanks go to Peter Keuschnigg from medPhoton for every advise and consultation. Thanks also to the whole medPhoton team around Phillip Steiniger as well as to Daniel Sieber for supervising the project.

References

[1] I. Goodfellow, Y. Bengio, and A. Courville, *Deep Learning*. MIT Press, 2016, http://www.deeplearningbook.org.

[2] D. Shen, G. Wu, and H.-I. Suk, "Deep learning in medical image analysis," *Annual review of biomedical engineering*, vol. 19, pp. 221–248, 2017. [Online]. Available: https://www.ncbi.nlm.nih.gov/pmc/articles/PMC5479722/

[3] J.-G. Lee, S. Jun, Y.-W. Cho, H. Lee, G. B. Kim, J. B. Seo, and N. Kim, "Deep learning in medical imaging: General overview," *Korean Journal of Radiology*, vol. 18, no. 4, pp. 570–584, 2017. [Online]. Available: https://www.ncbi.nlm.nih.gov/pmc/articles/PMC5447633/

[4] S. K. Zhou, H. Greenspan, C. Davatzikos, J. S. Duncan, B. van Ginneken, A. Madabhushi, J. L. Prince, D. Rueckert, and R. M. Summers, "A review of deep learning in medical imaging: Imaging traits, technology trends, case studies with progress highlights, and future promises," *Proceedings of the IEEE. Institute of Electrical and Electronics Engineers*, vol. 109, no. 5, pp. 820–838, 2021. [Online]. Available: https://www.ncbi.nlm.nih.gov/pmc/articles/PMC10544772/

[5] S. Russell and J. Bohannon, "Artificial intelligence. fears of an ai pioneer," *Science (New York, N.Y.)*, vol. 349, no. 6245, p. 252, 2015. [Online]. Available: https://www.science.org/doi/10.1126/science.349.6245.252?url

[6] C. Liew, "The future of radiology augmented with artificial intelligence: A strategy for success," *European Journal of Radiology*, vol. 102, pp. 152–156, 2018. [Online]. Available: https://www.sciencedirect.com/science/article/pii/S0720048X18301116

[7] J. Potočnik, S. Foley, and E. Thomas, "Current and potential applications of artificial intelligence in medical imaging practice: A narrative review," *Journal of Medical Imaging and Radiation Sciences*, vol. 54, no. 2, pp. 376–385, 2023. [Online]. Available: https://www.sciencedirect.com/science/article/pii/S1939865423000796

[8] Q. Yan, Y. Ye, J. Xia, Z. Cai, Z. Wang, and Q. Ni, "Artificial intelligence-based image reconstruction for computed tomography: A survey," *Intelligent Automation & Soft Computing*, vol. 36, no. 3, pp. 2545–2558, 2023. [Online]. Available: https://www.researchgate.net/publication/369328742

[9] K. Karthik and K. S. Sowmya, "Deep neural models for automated multi-task diagnostic scan management-quality enhancement, view classification and report generation," *Biomedical physics & engineering express*, vol. 8, no. 1, 2021. [Online]. Available: https://iopscience.iop.org/article/10.1088/2057-1976/ac3add

[10] *Nuclear Medicine Physics*, ser. Non-serial Publications. Vienna: INTERNATIONAL ATOMIC ENERGY AGENCY, 2015. [Online]. Available: https://www.iaea.org/publications/10368/nuclear-medicine-physics

[11] M. Abdullah-Al-Wadud, M. Kabir, M. Dewan, and O. Chae, "A dynamic histogram equalization for image contrast enhancement," *Consumer Electronics, IEEE Transactions on*, vol. 53, pp. 593 – 600, 06 2007. [Online]. Available: https://ieeexplore.ieee.org/document/4266947

[12] S. D. Chen and A. R. Ramli, "Contrast enhancement using recursive mean-separate histogram equalization for scalable brightness preservation," *Consumer Electronics, IEEE Transactions on*, vol. 49, pp. 1301 – 1309, 12 2003. [Online]. Available: https://ieeexplore.ieee.org/document/1261233

[13] K. J. Zuiderveld, "Contrast limited adaptive histogram equalization," in *Graphics gems*, 1994. [Online]. Available: https://api.semanticscholar.org/CorpusID:62707267

[14] X. Zhao, T. Zhang, H. Liu, G. Zhu, and X. Zou, "Automatic windowing for mri with convolutional neural network," *IEEE Access*, vol. 7, pp. 68 594–68 606, 2019. [Online]. Available: https://ieeexplore.ieee.org/document/8721686

[15] F. Tan, Y. Li, and M. Guan, "Automatic windowing for highly dynamic industrial x-ray image based on short-term energy of gray histogram," *Journal of Nondestructive Evaluation*, vol. 36, no. 3, 2017. [Online]. Available: https://link.springer.com/article/10.1007/s10921-017-0432-6

[16] C. Hoeschen, S. Reissberg, and W. Doehring, "Importance of optimizing the image processing for different digital x-ray detectors to get as much information as possible from the radiographs," in *Medical Imaging 2002: Physics of Medical Imaging*, ser. SPIE Proceedings, L. E. Antonuk and M. J. Yaffe, Eds. SPIE, 2002, pp. 828–838. [Online]. Available: https://www.spiedigitallibrary.org/conference-proceedings-of-spie/4682/1/Importance-of-optimizing-the-image-processing-for-different-digital-x/10.1117/12.465634.short

[17] A. Albiol, A. Corbi, and F. Albiol, "Automatic intensity windowing of mammographic images based on a perceptual metric," *Medical physics*, vol. 44, no. 4, pp. 1369–1378, 2017. [Online]. Available: https://aapm.onlinelibrary.wiley.com/doi/10.1002/mp.12144

[18] H. Yeganeh, Z. Wang, and E. R. Vrscay, "Adaptive windowing for optimal visualization of medical images based on a structural fidelity measure," in *Image Analysis and Recognition*, ser. Lecture Notes in Computer Science, D. Hutchison, T. Kanade, J. Kittler, J. M. Kleinberg, F. Mattern, J. C. Mitchell, M. Naor, O. Nierstrasz, C. Pandu Rangan, B. Steffen, M. Sudan, D. Terzopoulos, D. Tygar, M. Y. Vardi, G. Weikum, A. Campilho, and M. Kamel, Eds. Berlin, Heidelberg: Springer Berlin Heidelberg, 2012, vol. 7325, pp. 321–330. [Online]. Available: https://ece.uwaterloo.ca/ z70wang/publications/ICIAR12.pdf

[19] N. Nikvand, H. Yeganeh, and Z. Wang, "Adaptive windowing for optimal visualization of medical images based on normalized information distance," in *2014 IEEE International Conference on Acoustics, Speech and Signal Processing (ICASSP)*. IEEE, 2014, pp. 1200–1204. [Online]. Available: https://ieeexplore.ieee.org/document/6853787

[20] A. Ohhashi, S. Yamada, K. Haruki, H. Hatano, K. Nishimura, Y. Fujii, K. Yamaguchi, and H. Ogata, "Application of a neural network to automatic gray level adjustment for medical images," in *[Proceedings] 1991 IEEE International Joint Conference on Neural Networks*. IEEE, 1991, pp. 974–980 vol.2. [Online]. Available: https://ieeexplore.ieee.org/document/170526

[21] S. H. Lai and M. Fang, "A hierarchical neural network algorithm for robust and automatic windowing of mr images," *Artificial intelligence in medicine*, vol. 19, no. 2, pp. 97–119, 2000. [Online]. Available: https://pubmed.ncbi.nlm.nih.gov/10814906/

[22] S.-H. Lai and M. Fang, "An adaptive window width/center adjustment system with online training capabilities for mr images," *Artificial intelligence in medicine*, vol. 33, no. 1, pp. 89–101, 2005. [Online]. Available: https://pubmed.ncbi.nlm.nih.gov/15617983/

[23] D. Sundaran, D. Kulkarni, and J. Dholakia, "Optimal windowing of mr images using deep learning: An enabler for enhanced visualization." [Online]. Available: http://arxiv.org/pdf/1908.00822v1

[24] J. Ansel, E. Yang, H. He, N. Gimelshein, A. Jain, M. Voznesensky, B. Bao, P. Bell, D. Berard, E. Burovski, G. Chauhan, A. Chourdia, W. Constable, A. Desmaison, Z. DeVito, E. Ellison, W. Feng, J. Gong, M. Gschwind, B. Hirsh, S. Huang, K. Kalambarkar, L. Kirsch, M. Lazos, M. Lezcano, Y. Liang, J. Liang, Y. Lu, C. K. Luk, B. Maher, Y. Pan, C. Puhrsch, M. Reso, M. Saroufim, M. Y. Siraichi, H. Suk, S. Zhang, M. Suo, P. Tillet, X. Zhao, E. Wang, K. Zhou, R. Zou, X. Wang, A. Mathews, W. Wen, G. Chanan, P. Wu, and S. Chintala, "Pytorch 2: Faster machine learning through dynamic python bytecode transformation and graph compilation," in *Proceedings of the 29th ACM International Conference on Architectural Support for Programming Languages and Operating Systems, Volume 2*, D. Tsafrir, M. Musuvathi, R. Gupta, and N. Abu-Ghazaleh, Eds. New York, NY, USA: ACM, 2024, pp. 929–947.

[25] F. Pérez-García, R. Sparks, and S. Ourselin, "Torchio: A python library for efficient loading, preprocessing, augmentation and patch-based sampling of medical images in deep learning," *Computer methods and programs in biomedicine*, vol. 208, p. 106236, 2021.

[26] S. Pappenberger, "Ai-based window-leveling for x-ray images."

[27] H. Jiang, Y. Gu, Y. Xie, R. Yang, and Y. Zhang, "Solar irradiance capturing in cloudy sky days–a convolutional neural network based image regression approach," *IEEE Access*, vol. 8, pp. 22 235–22 248, 2020. [Online]. Available: https://ieeexplore.ieee.org/document/8970273

[28] J. T. Bushberg, J. A. Seibert, E. M. Leidholdt, and J. M. Boone, *The essential physics of medical imaging*, 3rd ed. [Place of publication not identified]: LWW, 2011.

Sonja Pappenberger is with the Department of Medical and Health Technologies, MCI, Innsbruck, Austria.

APPENDIX A
IMAGE PRE-PROCESSING

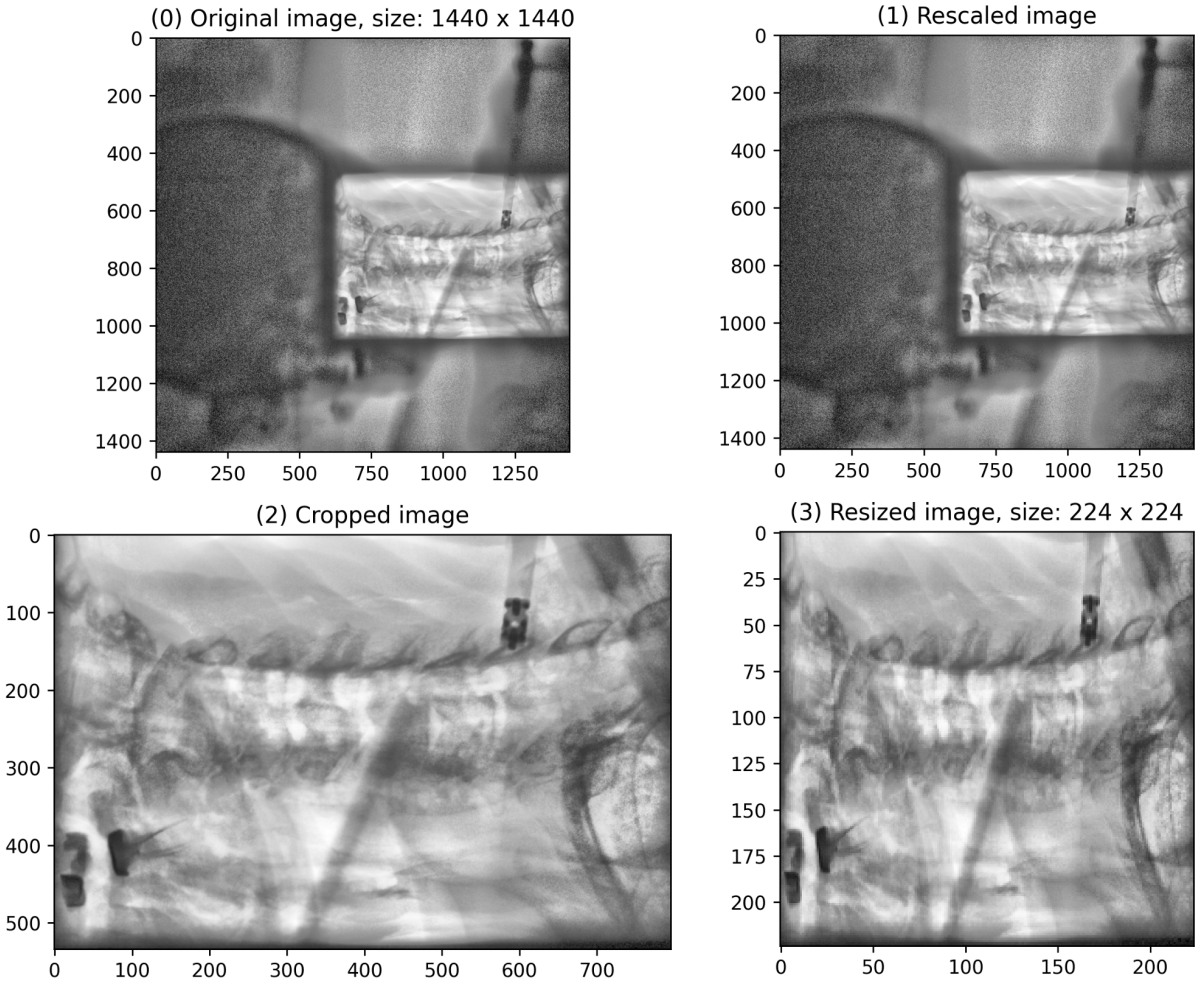

Fig. 2: Image pre-processing steps. Note that rescaling in the first step is not visible as the intensity pixel values were only linearly transformed.

APPENDIX B
COMPARISON OF LABEL AND PREDICTED VALUES

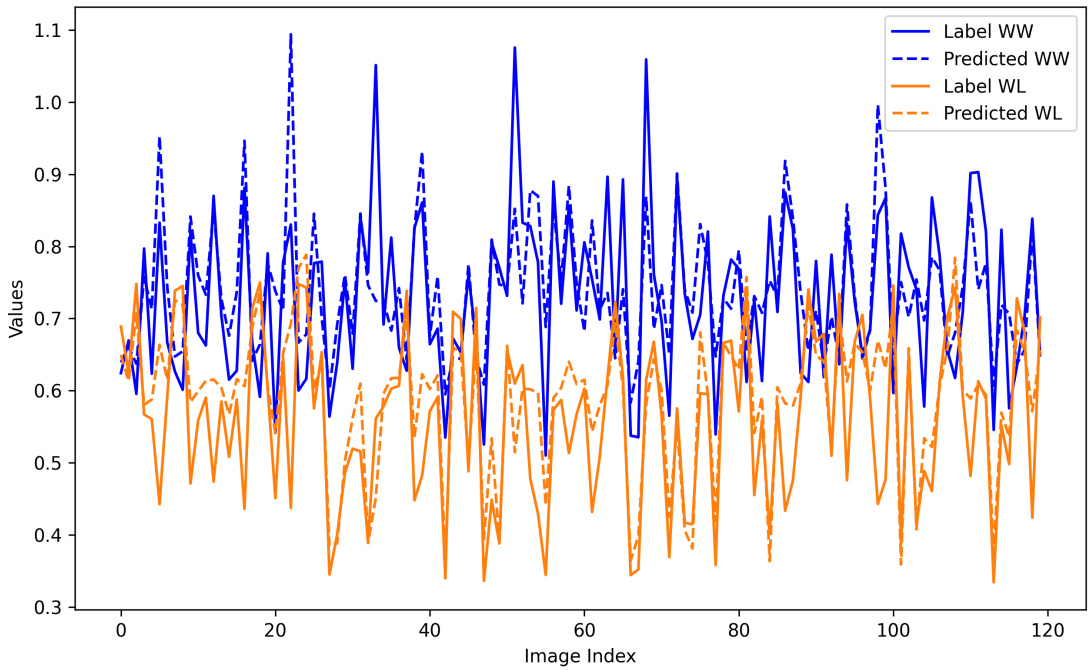

Fig. 3: Comparison between the label and the predicted values: The solid line presents the label window-leveling values computed by the AWL algorithm and the dotted line presents the values predicted by the baseline model.

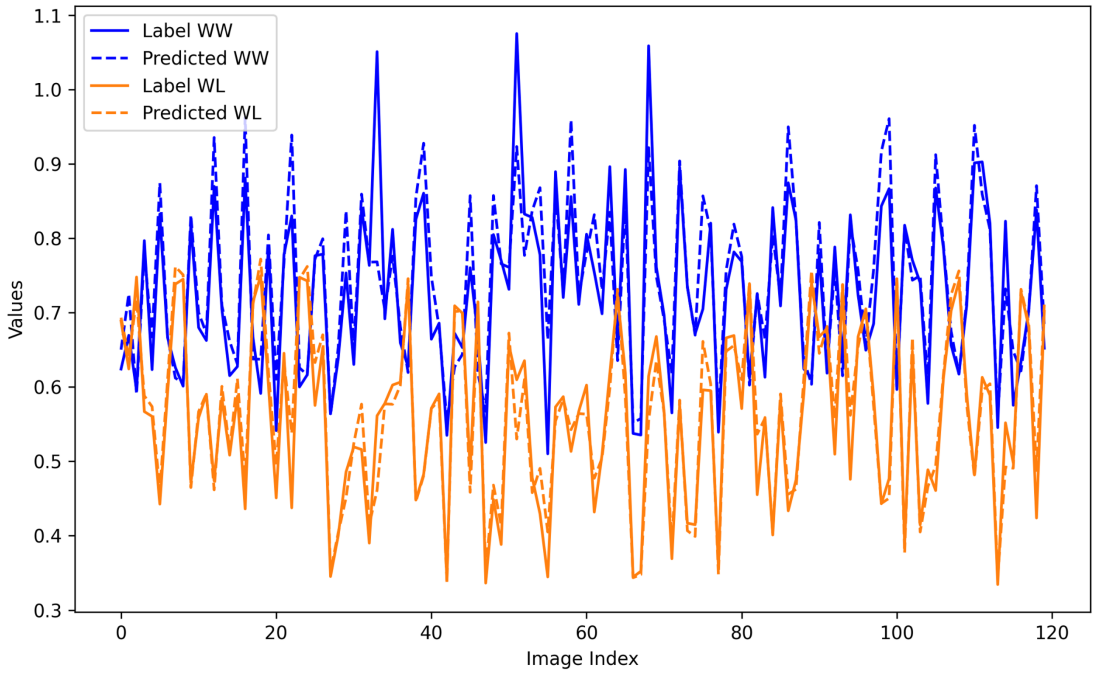

Fig. 4: Comparison between the label and the predicted values: The solid line presents the label window-leveling values computed by the AWL algorithm and the dotted line presents the values predicted by the model trained with optimized hyperparameter.

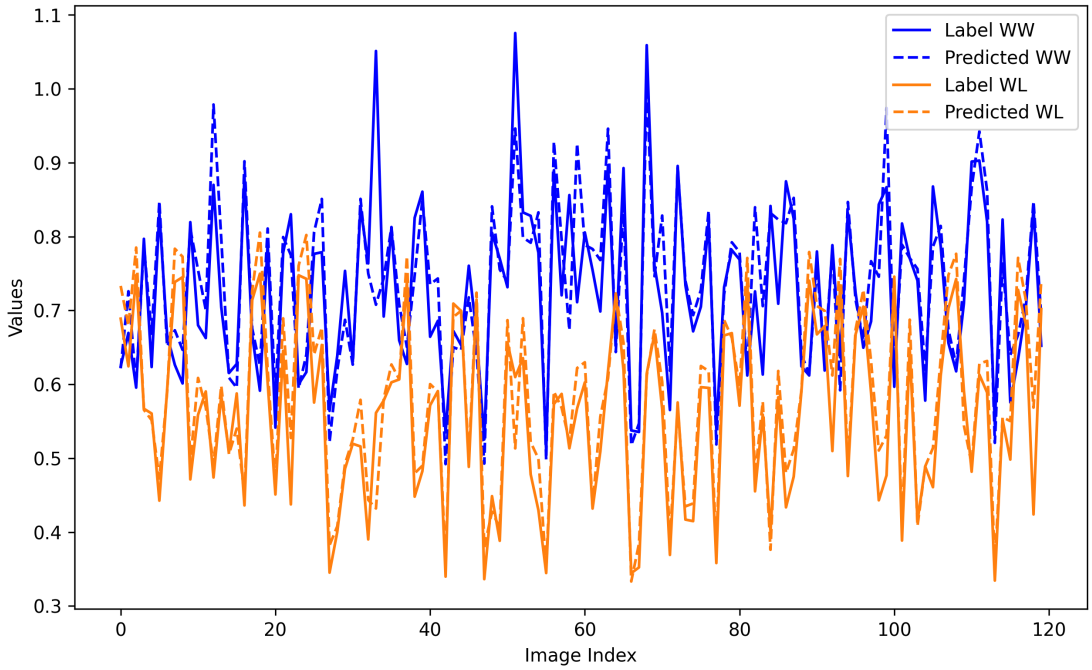

Fig. 5: Comparison between the label and the predicted values: The solid line presents the label window-leveling values computed by the AWL algorithm and the dotted line presents the values predicted by the downsized model (version E).

APPENDIX C
EXAMPLE X-RAYS

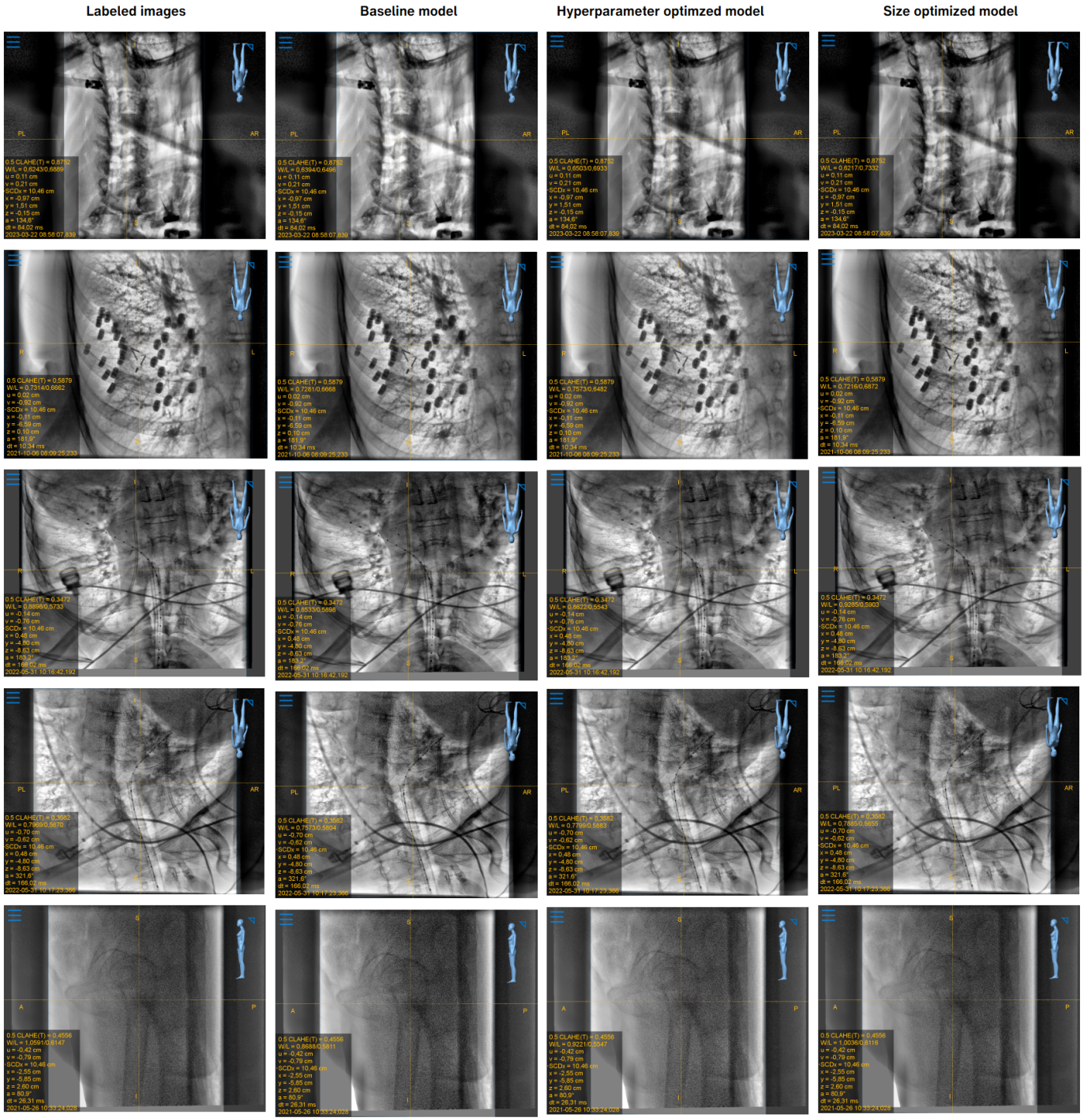

Fig. 6: Example x-rays visualized with the label and the predicted window-leveling parameters. *Left column:* X-rays visualized with label values. *Left middle row:* X-rays visualized with parameters predicted by baseline model. *Right middle column:* X-rays visualized with parameters predicted by the model with optimized hyperparameters. *Right column:* X-rays visualized with parameters predicted by the model with optimized size.

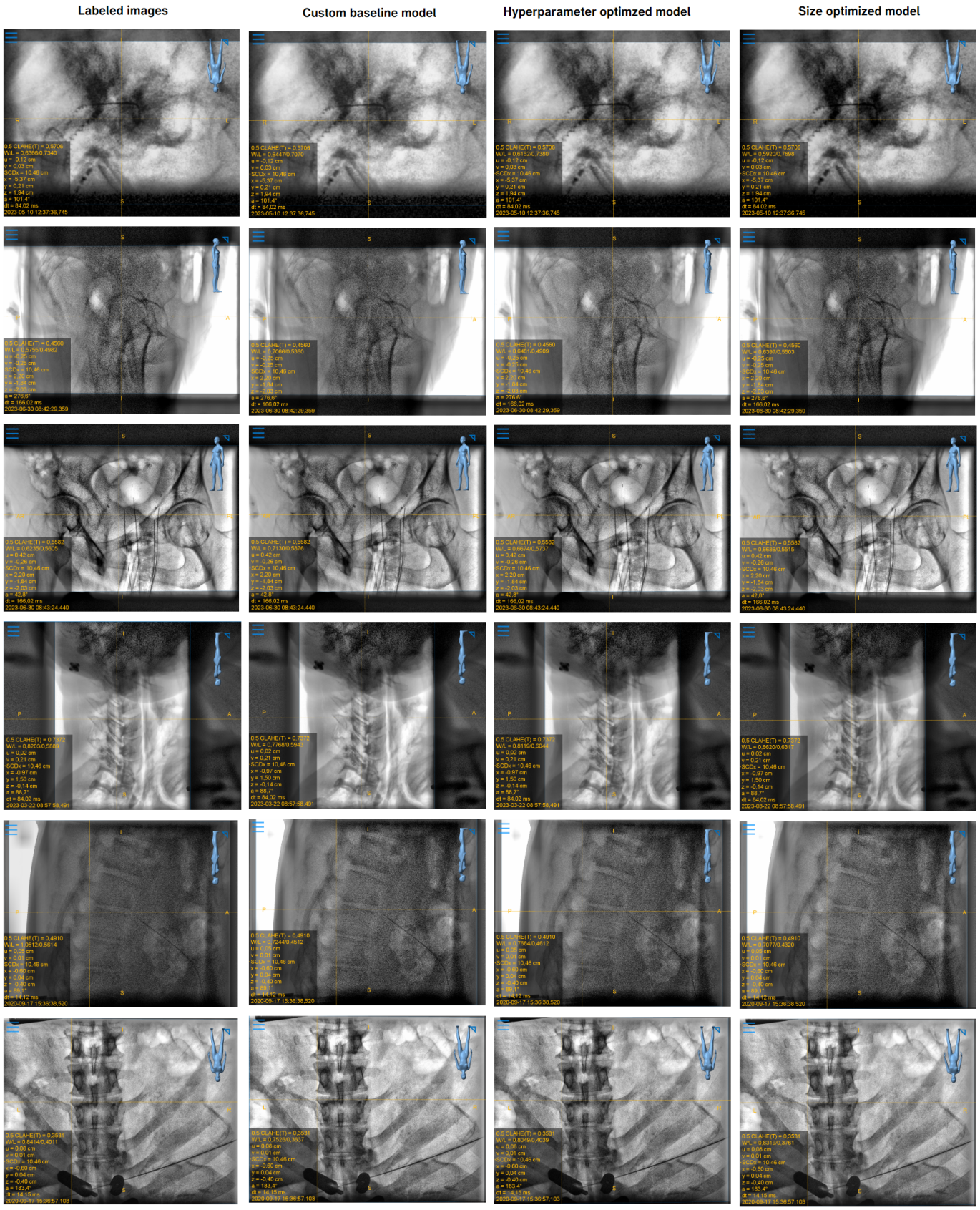

Fig. 6 (continued): Example x-rays visualized with the label and the predicted window-leveling parameters. *Left column:* X-rays visualized with label values. *Left middle row:* X-rays visualized with parameters predicted by baseline model. *Right middle column:* X-rays visualized with parameters predicted by the model with optimized hyperparameters. *Right column:* X-rays visualized with parameters predicted by the model with optimized size.